Additive Manufacturing Letters 6 (2023) 100150

Contents lists available at ScienceDirect

Additive Manufacturing Letters

journal homepage: www.elsevier.com/locate/addlet

Short Communication

A close look at temperature profiles during laser powder bed fusion using operando X-ray diffraction and finite element simulations

Pooriya Scheel[a,b], Patrik Markovic[a,b], Steven Van Petegem[c], Malgorzata Grazyna Makowska[d], Rafal Wrobel[a,e], Thomas Mayer[f], Christian Leinenbach[a,g], Edoardo Mazza[a,b], Ehsan Hosseini[a,*]

[a] Empa Swiss Federal Laboratories for Materials Science & Technology, Überlandstrasse 129, Dübendorf 8600, Switzerland
[b] ETH Zürich, Department of Mechanical and Process Engineering, Institute for Mechanical Systems, Leonhardstrasse 21, Zürich 8092, Switzerland
[c] Paul Scherrer Institut, Structure and Mechanics of Advanced Materials, Villigen 5232, Switzerland
[d] Paul Scherrer Institut, microXAS group & Advanced Nuclear Materials group, Villigen 5232, Switzerland
[e] ETH Zürich, Department of Materials, Laboratory for Nanometallurgy, Vladimir-Prelog-Weg 4, Zürich 8093, Switzerland
[f] ZHAW School of Engineering, Institute of Mechanical Systems, Technikumstrasse 9, Winterthur 8401, Switzerland
[g] École Polytechnique Fédérale de Lausanne (EPFL), Laboratory for Photonic Materials and Characterization, Lausanne 1015, Switzerland

ARTICLE INFO

Keywords:
Laser powder bed fusion
Finite element thermal analysis
Operando X-ray diffraction

ABSTRACT

In laser powder bed fusion (LPBF), complex components are manufactured layer-by-layer via scanning the cross-sections of a 3D CAD model using a high intensity laser. Throughout this process, the material is exposed to temperature profiles that significantly differ from conventional manufacturing methods, and result in development of a unique and inhomogeneous microstructure and high levels of residual stresses in additively fabricated parts. The large temperature gradients and rapid cooling rates around the moving laser spot, and the overall heterogeneity of the temperature field need to be better understood in order to optimize the process parameters for increased production quality. In this study, *operando* X-ray diffraction (XRD) was employed to measure and compare temperature histories on the laser path under various processing conditions for Hastelloy X. Finite element thermal simulations were validated based on the acquired XRD data and then used as a supplementary tool to discuss the cooling behaviour and thermal heterogeneities across the geometry. The increase in the deposited energy density was qualitatively linked with higher temperature levels and slower cooling rates during LPBF. The melt-pool lengths showed strong sensitivity to the laser power and little variation with the scanning speed. Furthermore, even for a single set of parameters, large variations in the temperature field within the build were observed such that the cross-section edges located at higher build layers were exposed to markedly higher temperature levels.

1. Introduction

Applications of metal additive manufacturing (MAM) technologies have been rapidly growing over the recent decades thanks to various benefits such as increased design freedom for complex geometrical features, reduced total production time and efficient usage of raw materials [1,2]. It is known that the microstructure, properties and internal/residual stress state of AM products are very different to conventionally manufactured parts [3–5]. Further understanding of the complex physics involved in MAM and correlations to the process parameters is required to improve the characteristics of produced components and reach the goal of first-time-right high quality manufacturing. One of the most important differences of a MAM method such as laser powder bed fusion (LPBF) with traditional counterparts lies in the thermal history experienced by the material during the build process [6]. In LPBF, a high-intensity laser scans cross-sections of a geometry over layers of powder, where large temperature gradients with rapid transience develop in the vicinity of the process zone. The resulting temperature field is highly sensitive to parameters such as the laser power and the scanning speed, which in turn cause variations in the microstructure and mechanical properties of printed parts [7–9]. Even for a single set of parameters, heterogeneities across the fabricated geometry have shown a large impact on the melt-pool dimensions and the local microstructure of builds [10–12].

The thermal history can be studied via conventional temperature measurement techniques, but the small space- and time-scale of the process pose certain challenges. For instance, thermocouples have been used to monitor the temperature evolution during LPBF [13–15]. However, they are often placed relatively far from the laser tracks and sampled at low frequencies (e.g. 1 kHz) which make it difficult to gather in-

* Corresponding author.
E-mail address: ehsan.hosseini@empa.ch (E. Hosseini).

https://doi.org/10.1016/j.addlet.2023.100150
Received 22 March 2023; Received in revised form 5 May 2023; Accepted 21 May 2023

formation about the thermal evolutions in the process zone. On the other hand, if placed too close to laser tracks, they may get burned and damaged during the measurement [16]. Another way is to use high-speed infra-red [17,18] or visible light [19,20] cameras to measure temperatures in their corresponding radiation wavelength ranges. While high frequency data acquisition in these methods (e.g. 100 kHz) provides good temporal resolution, deriving temperature values from observed intensities requires reliable information about emissivities of the printed alloy in solid, liquid, and powder state which are not readily available. Furthermore, plume formation over the process zone from metal evaporation can block the view of the camera and increase measurement uncertainties [19,20].

In this work, an alternative technique using *operando* X-ray diffraction (XRD) was employed to measure the changes in atomic spacing of material during LPBF and correlate it to temperature evolutions based on thermal expansion behaviour of the material [21]. The test setup involves a miniaturized selective laser melting (miniSLM) machine which has been specifically developed for usage in synchrotron beamlines [22]. Previously, by analysing XRD peaks from LPBF of Ti6Al4V, the feasibility of high resolution temperature measurements in the evolving process zone has been demonstrated [21]. In the present study, diffraction patterns were collected during LPBF of Hastelloy X (HX) under a variety of process conditions to study the effect of process parameters on temperature profiles. Since HX is a single phase alloy, the continuity of temperature history in the solid state was maintained and no complications from phase transitions (e.g. α/β transformation in Ti6Al4V) were involved. HX is a Ni-based superalloy with great oxidation-resistance and high-temperature strength [23], which make it a fitting choice for complex components in gas turbines [24] and heat exchangers [25], particularly in combination with design and fabrication flexibility of MAM.

The X-ray temperature measurement has certain drawbacks, such as the limitation to a single spot and availability of the data only in the solid state. This motivated the development of accompanying finite-element (FE) simulations, which were used to complement the XRD measurements, after corresponding calibration and validation. Importantly, the XRD-FE combination facilitated the determination of cooling rates, and evaluation of heterogeneities in the temperature field induced by geometrical factors.

2. Methodology

2.1. Operando X-ray diffraction

Operando XRD measurements in LPBF were conducted at the microXAS beamline in the Swiss Light Source at Paul Scherrer Institute using the miniSLM machine [26]. The device was equipped with a 12 mm × 12 mm build-stage between two glassy carbon windows which block infra-red and visible light but transmit X-ray beams [26]. The machine was tilted 17° with respect to a horizontal axis (Y-axis in Fig. 1a) to expose the powder bed to the incoming X-ray beam and enable diffraction in reflection mode. The incline was set below the 'angle of repose' of most powders (i.e. 20°) to ensure the deposited powder layers are stable [22]. The 17.5 keV monochromatic X-ray beam was focused down to 110 μm × 41 μm (reported as full-width-tenth-maximum) which corresponds to an illuminated area of 110 μm × 140 μm on the tilted surface. The exiting scattered X-ray radiation was recorded using an EIGER 1M detector at a frequency of 20 kHz [27]. A schematic of the set-up is provided in Fig. 1a and the machine placement in front of the beamline is shown in Fig. 1b. For the print jobs, gas-atomised HX powder with an average particle size of 30 μm was used and the nominal composition is reported in Table A.1 (in supplementary materials). From the same alloy, customized build-plates with 2 mm thickness were machined. The design allowed for spot-welding a thermocouple pair underneath the build-plate whose reading was used in model calibration.

Prior to beamline experiments, various combinations of laser power, scanning speed, and hatch spacing were tested to find the optimum process parameters for good visual surface quality (sample 1 in Table 1). The *in-situ* measurements started with LPBF of 1 mm × 8 mm rectangles over 11 layers using the reference parameters (sample 1). Next, the laser power P (in samples 2 and 3), and scanning speed V (in samples 4 and 5) were changed one at a time to fabricate the same geometry. Then, these two parameters in combination with hatch spacing H were altered such that the volumetric energy density E_v defined as the following was kept constant (samples 6 and 7):

$$E_v = \frac{P}{VH\delta} \tag{1}$$

where δ is the powder layer thickness. An overview of the process parameters across various tests are provided in Table 1, and the common settings are reported in Table 2. At the end of each print job, the top layer was rescanned, and XRD patterns were collected for the remelting process. The resulting data provided higher quality diffraction patterns compared to scanning powder layers, and was used for validating the simulation results.

Data collection for each layer deposition was triggered by laser activation and lasted for 1 second, covering the entire scanning duration and approximately 0.7 second of cooling. With the 20 kHz sampling rate, a sequence of 20'000 diffraction patterns were recorded per measurement. Each frame was reduced to a 1D profile with azimuthal integration as shown in Fig. 2a, where characteristic peaks for a face centred cubic crystal structure are observed. The measurement data for one layer deposition can be represented as a 2D image by stacking the times series of 1D profiles as shown in Fig. 2b. The start of the measurement corresponds to reflections off the powder particles (e.g. at $t = 0$ ms in Fig. 2a), and as soon as the laser scans over them, rapid shifts in peak position are observed (e.g. at $t = 114$ ms in Fig. 2a). These diffraction angles are related to the atomic distances of the crystalline material in build-direction (Z-axis), which vary due to thermal expansion as the laser scans over and around the X-ray probed region. Using Bragg's law, lattice strains were calculated based on the shift in peak positions, which could then be used to calculate the temperature evolutions based on thermal expansion behaviour of the alloy. While the small size of the probed volume has the advantage of providing high spatial resolution in the measurements, it can result in poor grain statistics and make reliable diffraction analysis difficult. In most cases, the peaks corresponding to (220) or (311) crystal planes were more pronounced, but for better consistency primarily the (220) peaks were used in post-processing.

2.2. Data analysis

The time evolution of peak angles 2θ were calculated from 1D diffraction data based on a weighted average over a 0.4° range around the maximum intensities. Following Bragg's law, the lattice strains ε_l can be written in terms of 2θ as [21]:

$$\varepsilon_l(t) = -\cot\left(\frac{2\theta(t)}{2}\right)\frac{2\theta(t) - 2\theta_0}{2} \tag{2}$$

where $2\theta_0$ is the diffraction angle corresponding to the chosen peak at a reference state for the crystal, which could be defined based on the diffraction data from the beginning or the end of each measurement. The former option was faced with issues related to variations in the sample-detector distance before and after the consolidation of powder particles. The significant vertical drop in the build surface height (up to 3× the nominal powder layer thickness [28,29]) caused unfavorable shifts in diffraction rings on the detector. However, the latter choice ensured spatial consistency, and the average of peak positions in the last 5 ms of each measurement was used to define $2\theta_0$. The evolution of residual stresses during the measurement can affect the crystal lattice, but the impact on the process zone temperature measurements through XRD was estimated to be negligible (as demonstrated in Fig. A.1 in supplementary materials). Furthermore, it is also recognized the scanned area

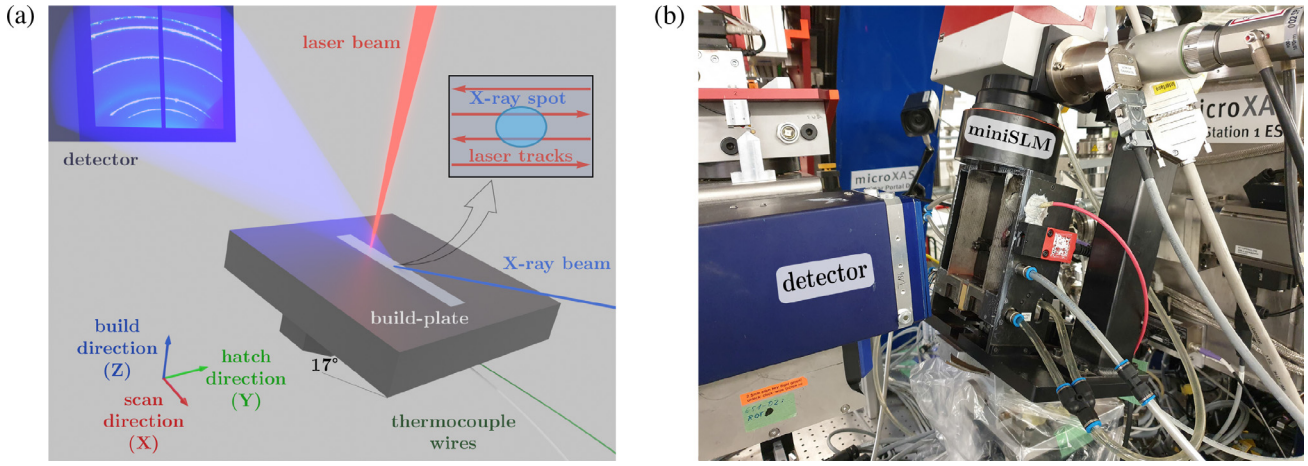

Fig. 1. The measurement setup. (a) A schematic showing how build-plate was tilted to enable diffraction measurements in reflection mode. (b) The miniSLM machine mounted at the microXAS beamline.

Table 1
Varied process parameters across samples and corresponding volumetric energy densities.

Sample	Laser power P (W)	Scanning speed V (mm/s)	Hatch distance H (μm)	Volumetric energy density E_v (J/ mm^3)
1	300	700	70	204 (reference)
2	250	700	70	170 (−17 %)
3	350	700	70	238 (+17 %)
4	300	500	70	286 (+40 %)
5	300	900	70	159 (−22 %)
6	250	510	80	204 (0 %)
7	350	950	60	204 (0 %)

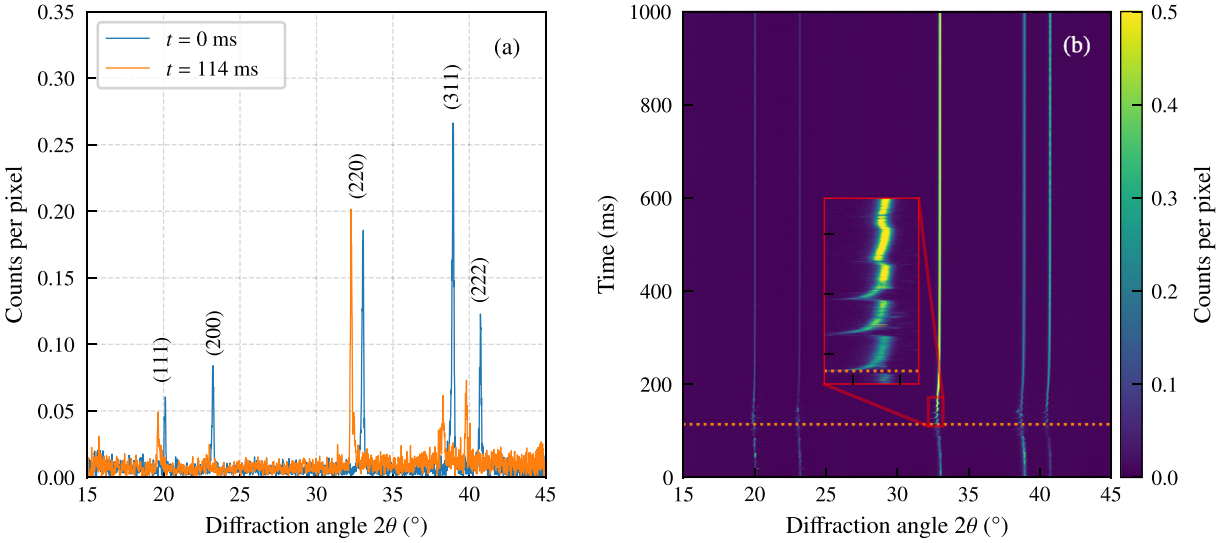

Fig. 2. XRD patterns collected during scanning the first layer of sample 1. (a) 1D diffraction pattern of powder particles at 0 ms and solid at 114 ms with shifted peaks due to an increase in temperature. The changes in peak intensity are attributed to variations in grain statistics. (b) Rasterized 2D representation of all collected 1D diffraction patterns in this measurement. The inset highlights oscillations in peak diffraction angles with repeated exposure to the moving laser indicating the changes in lattice spacing with temperature. t = 114 ms corresponding to (a) is indicated by the horizontal dotted line.

Table 2
Common settings used across all measurements.

Parameter	Value
Laser spot size d_{laser} (μm)	55
Powder layer thickness δ (μm)	30
Scanning strategy	Bidirectional

of the assumed reference state would be slightly warmer than the ambient (i.e. $T(1\text{s}) > 25°\text{C}$). This temperature increase was estimated to be up to 50°C, and was accounted for by exploring FE results. Ultimately, by assuming that the changes in lattice spacing are predominantly caused by thermal effects, we can write:

$$T(t) - T(1\text{s}) \approx \frac{\epsilon_l(t)}{\alpha_L(T)} \tag{3}$$

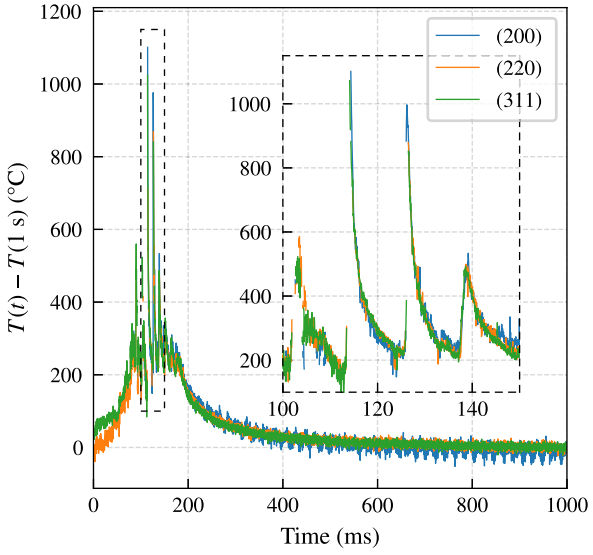

Fig. 3. Characteristics temperature profiles based on XRD analysis from different crystal planes during deposition of the 1st layer of sample 2.

where $T(t)$ is the temperature evolution in the probed region, and $\alpha_L(T)$ is the coefficient of linear thermal expansion. Thermal expansion behaviour of HX over the 23°C to 1100°C range was determined by dilatometry of LPBF fabricated specimens (measurement results are provided in Fig. A.2 in supplementary materials). Then, a cubic polynomial fit was used to directly represent T as a function of ε.

Typical temperature histories based on different crystal planes are shown in Fig. 3. Since variations in temperatures calculated based on different crystal planes were small, the peaks corresponding to the previously mentioned (220) crystal planes were used to report the temperature measurements in the following. As noted earlier, while the XRD measurements provide high resolution data over a wide range of temperatures, they are limited to a single spot and the time series becomes discontinuous during liquid formation (due to lack of a crystal structure in liquid state for diffraction). Moreover, reliably estimating time-derivative of temperature profiles is difficult due to overall noise in the measurement data. To complement the experiments and further study the thermal evolutions in LPBF, the measurements were combined with simulations, which provided a continuous and smooth temperature field over the entire domain. The set-up of the model and its validation are presented next.

2.3. Finite-element simulations

The FE thermal models of LPBF were setup in Abaqus 2021 following continuum assumptions similar to [30–34]. In this scheme, the powder layer is modelled as continuum media with equivalent properties and the phenomena related to liquid metal formation and motion are ignored. Accordingly, the following heat conduction equation was solved for the transient temperature distribution $T(x, y, z, t)$ using the Abaqus/Standard algorithm:

$$\rho c_p \dot{T} - \nabla \cdot (k \nabla T) = q_{\text{vol}} \tag{4}$$

where ρ is the density at room temperature 25°C and was measured to be 8352 kg/m^3 ± 2% for LPBF-fabricated HX specimens [35], k and c_p are the (effective) temperature-dependent thermal conductivity and specific heat capacity of the material, respectively, and q_{vol} is the volumetric moving heat source from laser exposure. In a previous study, differential scanning calorimetry was used to measure the effective specific heat capacity of LPBF HX samples, which represents both the specific heat capacity and enthalpy changes due to the latent heat of fusion (in the 1357.6°C to 1399.5°C range) and an exothermic effect (in the 430°C to 620°C range) [35]. In addition, the thermal diffusivity of LPBF fabricated specimens was measured using laser flash analysis in the 20°C to 1100°C range and linearly extrapolated to the solidus temperature of 1357.6°C. To account for increased heat transfer by convection in the melt-pool due to fluid motion, the thermal conductivity in the liquid state was considered to be 15 times larger than the solid thermal conductivity at the solidus temperature, i.e. $k_{\text{liq}} = 15 \times k_{sld}(T = 1357.6°\text{C})$ similar to [33]. Lastly, the thermal conductivity of the powder state was assigned as 5 % of the bulk solid material [36]. The temperature-dependent material properties are provided in Fig. A.3 in supplementary materials.

The moving heat source term q_{vol} in Eq. (4) was implemented by a simplified representation of the Goldak formulation [37]:

$$q_{\text{vol}} = \eta \frac{6\sqrt{3}P}{r^2 \delta \pi \sqrt{\pi}} \exp\left(-\frac{3(x^2+y^2)}{r^2} - \frac{3z^2}{\delta^2}\right) \tag{5}$$

where P is the laser power, η is the laser absorption coefficient, r is the laser spot radius (27.5 µm) and δ is the powder layer thickness (30 µm). The x, y and z spatial coordinates are defined locally for a moving coordinate system centred on the laser heat source, such that its X-axis is aligned with the scan direction. The remaining unknown variable η was challenging to measure directly. Thus, the far-field temperature history beneath the build-plate was recorded by a K-type thermocouple pair, which represents the overall energy input by the laser over multiple layer-depositions. Through a calibration process for η based on the temperatures measured by the thermocouple, an average value of 26 % was found to provide the best fit. Further information about this procedure is provided in Fig. A.5 in supplementary materials.

The model geometry consisted of the entire build-plate and the printed cuboid, where element activation for deposition of new layers was handled by the Abaqus AM modeller plug-in based on the 'quiet element method' [38]. An overview of the model and the mesh configuration using hexahedral linear elements can be found in Fig. A.4 in supplementary materials. In the process zone, 80 µm × 70 µm × 30 µm (reported along $x \times y \times z$-axes) elements similar in size to the X-ray probed area were used, which allowed for comparison of the simulations with the measurements by averaging the temperature history over the element nodes. To moderate the computational costs, larger elements were employed in other regions. A lumped film coefficient of 25 Wm^{-2}K^{-1} with an ambient temperature of 25°C was applied over all surfaces to emulate heat loss to the surrounding powder-bed [35]. A constant boundary temperature of 25°C was applied at the bottom of the build-plate stem, and the same value was used as the initial temperature over the whole domain.

2.4. Model validation

The FE simulations were validated based on XRD measurements to assess the relevance of model predictions. For this purpose, the high quality data acquired during the remelting process of different samples were used. The exact position of the X-ray probed region was determined by detailed assessment of XRD time series data (a visual representation of the procedure is provided in Fig. A.6, and the spatial offsets are reported in Table A.2 in supplementary materials). To quantify the closeness of model predictions to the measurements, the average of root-mean-square error (RMSE) and the coefficient of determination (R^2) across all 7 samples were determined to be 28.6°C (STD: 2.1°C) and 95.0 % (STD: 1.3 %), respectively. The model response for sample 1 and the corresponding measured temperature history is shown in Fig. 4, and additional cases are provided in Fig. A.7 and Table A.2 in supplementary materials, which indicate good agreement with the experiments.

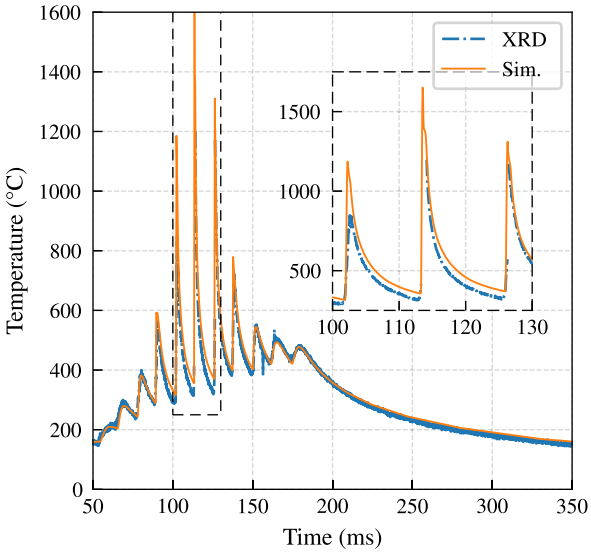

Fig. 4. Comparison of the simulation response with measured temperatures for remelting the top layer of sample 1.

3. Results and discussion

3.1. Process parameter variation

The parameter sets of Table 1 can be divided into three groups: (I) constant scanning speed and variable laser power in samples 1,2,3; (II) constant laser power and variable scanning speed in samples 1,4,5; and (III) constant volumetric energy density and variable laser power, scanning speed, and hatch distance in samples 1,6,7. Following this categorization, the XRD measured and FE simulated temperatures, and the calculated temperature evolution rates are shown in Fig. 5. It should be noted that the curves were shifted in time to assign $t = 0$ ms as the onset of heating and facilitate comparisons. As seen in Fig. 5d to 5f, the models provide information on the temperatures above the melting point (indicated by the horizontal dashed lines) where no XRD data was available. The variations in maximum recorded temperatures in Fig. 5a to 5c from XRD can be related to poor grain statistics immediately after solidification when the X-ray illuminated region has not fully crystallized to provide reliable diffraction patterns. Furthermore, these values are on average below the solidus temperature of 1357.6°C potentially from under-cooling in the melt-pool due to extremely high cooling rates in the process.

Cubic splines were fitted to simulated temperature histories for different samples using the scipy python library, and their first derivative was considered as cooling rate and shown in Fig. 5g to 5i. The cooling behaviour is characterized by two local extrema around solidification. The maxima indicates a slow-down in cooling caused by the release of the latent heat of fusion [19]. Shortly after the material has fully solidified, the largest cooling rates in the 0.7 $\times 10^6$K/s to 1.2 $\times 10^6$K/s range were observed which are in good agreement with previous measurements for LPBF of IN625 [18]. An overview of peak temperatures and cooling rates observed in simulations of different samples is provided in Table 3.

In the first group, the changes in measured temperatures with laser power are shown in Fig. 5a, and the simulation results can be seen in Fig. 5d. Overall, the temperatures are directly proportional to the laser power and consequently the energy density. However, the measurements after $t = 1.5$ ms show a larger temperature difference between P:300–350 W than P:250–300 W (Fig. 5a), while this effect is missing in the simulations (Fig. 5d) as the shift in curves remains almost identical. This discrepancy can be attributed to increased laser absorption efficiency for the higher laser power due to a transition towards keyhole welding [39,40], which was not taken into account for the models. It can be further observed that the cooling rate is the largest for the sample with the lowest power in Fig. 5g. With constant scanning speed, the decrease in power translates to deposition of less thermal energy and relatively colder material which can dissipate the heat faster. At $t = 1.5$ ms in Fig. 5g, whereupon the heat source has moved only 1mm away from the probed region, the rate curves quickly converge.

Table 3
Thermal characteristics of process zone temperature profiles. The cooling rate is reported for the post-solidification portion of the temperature curves.

Sample	T_{max} (°C)	Maximum Cooling-rate($\times 10^6$K/s)	Melt-pool Length (μm)
1	1658	1.03	368
2	1618	1.15	284
3	1722	0.87	482
4	1706	0.76	421
5	1637	1.32	345
6	1626	0.86	306
7	1707	1.13	431

In the next group of samples in Fig. 5b and 5e, the temperature levels show an inverse relationship with the scanning speed. The reduction in laser absorption efficiency at lower energy densities that was discussed for group (I) can be observed here as well. In particular, the increase in scanning speed shows a higher impact on temperature profiles in XRD measurements (Fig. 5b) than the model predictions (Fig. 5e). Nevertheless, in terms of magnitudes both the measurements and simulations show a larger shift for the 200 mm/s decrease in scanning speeds compared to increasing it by the same amount. This behaviour can be explained better by considering the volumetric energy density, which sees a larger increase with lowering the scanning speed through the inverse relationship $E_v \propto 1/V$. The cooling rates in Fig. 5h are inversely proportional to energy density similar to the trend observed for group (I). In this case, the quicker the heat source moves away from the probed area, the faster the material can cool down. E.g. at $t = 1$ ms in sample 5 (V=900 mm/s) the temperature has already fallen below 1000°C, while in sample 4 (V=500 mm/s) the material has just fully solidified, as the slower moving heat source is still in its close vicinity.

In the last group (Fig. 5c and 5f), where the volumetric energy density is kept constant, the shifts in temperature profiles are smaller than the previous two cases. When focusing on the thermal behaviour over a few milliseconds after exposure to laser, the distance between tracks is inconsequential and the P/V ratio (representing the linear energy density) can explain the variations better. Relative to sample 1 (green curve in Fig. 5c and 5f), this parameter changes by +14 % and −14 % for sample 6 (blue curve) and sample 7 (red curve), respectively. Thereby, the increase in P/V is accompanied by higher temperature levels in both XRD measurements (Fig. 5c) and simulations (Fig. 5f), and slower cooling rates in Fig. 5i.

The simulated temperature histories can be further explored for estimating the melt-pool length. Specifically, the time period between intersections of the temperature curve with the solidus line in Fig. 5d to 5f was multiplied with the corresponding scanning speed to determined the length of the molten region. The results for different samples are compared in Fig. 6, with dashed lines indicating contours of constant P/V, and absolute values are reported in Table 3. While the temperature levels were sensitive to both the laser power and scanning speed and consequently the deposited energy density, the melt-pool length shows a stronger correlation with the laser power. For instance, the red circle representing sample 7 (431 μm) is the second longest melt-

pool, even though it corresponds to a low P/V ratio. This result is in line with experimental observations by Keshavarzkermani et al. [7] that laser intensity has a larger impact on melt-pool dimensions compared to the scanning speed. However, it should be noted that changes in process parameters not only affect the melt-pool size, but also its ellipsoidal shape as the proportionality among different dimensions vary. For instance, Lane et al. [18] observed that increasing both the laser power and scanning speed may result in an elongated melt length, while shrinking the width and depth parameters, hence creating a narrow oval profile.

3.2. Geometry factors

The thermal history exposed to the material in LPBF is not only affected by process parameters such as laser power and scanning speed, but also by factors associated with the evolving geometry during the build process, which induce heterogeneities in the temperature field. One such element is the increasing build height as demonstrated by comparing the XRD measurements over the 1st and 11th (last) layer of sample 1 in Fig. 7a. A similar behaviour was predicted by the simulations in Fig. 7b, and the cooling rates decreased with increased layer number. Multi-layer deposition in LPBF generally causes heat accumulation in the component as the build process progresses, but with a relatively long recoating duration of ≈13 s in the miniSLM machine, the thermal energy from previous layers mostly dissipates before the start of a new layer. More importantly, the larger distance between the process zone and the build-plate at higher layers increases the thermal resistance which impedes conductive heat dissipation and increases the temperature levels. Thus, the observed difference in temperature histories between layer 1 and 11 developed only from the deposited thermal energy in the current layer. It should be noted that these changes are associated with only a 0.3 mm increase in build height. A larger difference in temperatures would be expected for bigger prints. Particularly, a shorter recoating duration increases the gradual heating of the part as well, and further reduces the cooling rates, as indicated by reported inhomogeneities in the microstructure where coarser grains were observed at higher sections of fabricated parts [41].

In addition to build height, the temperature profiles within the same layer are expected to be heterogeneities due to the changes in the local heat transfer conditions. While this aspect could not be explored in the

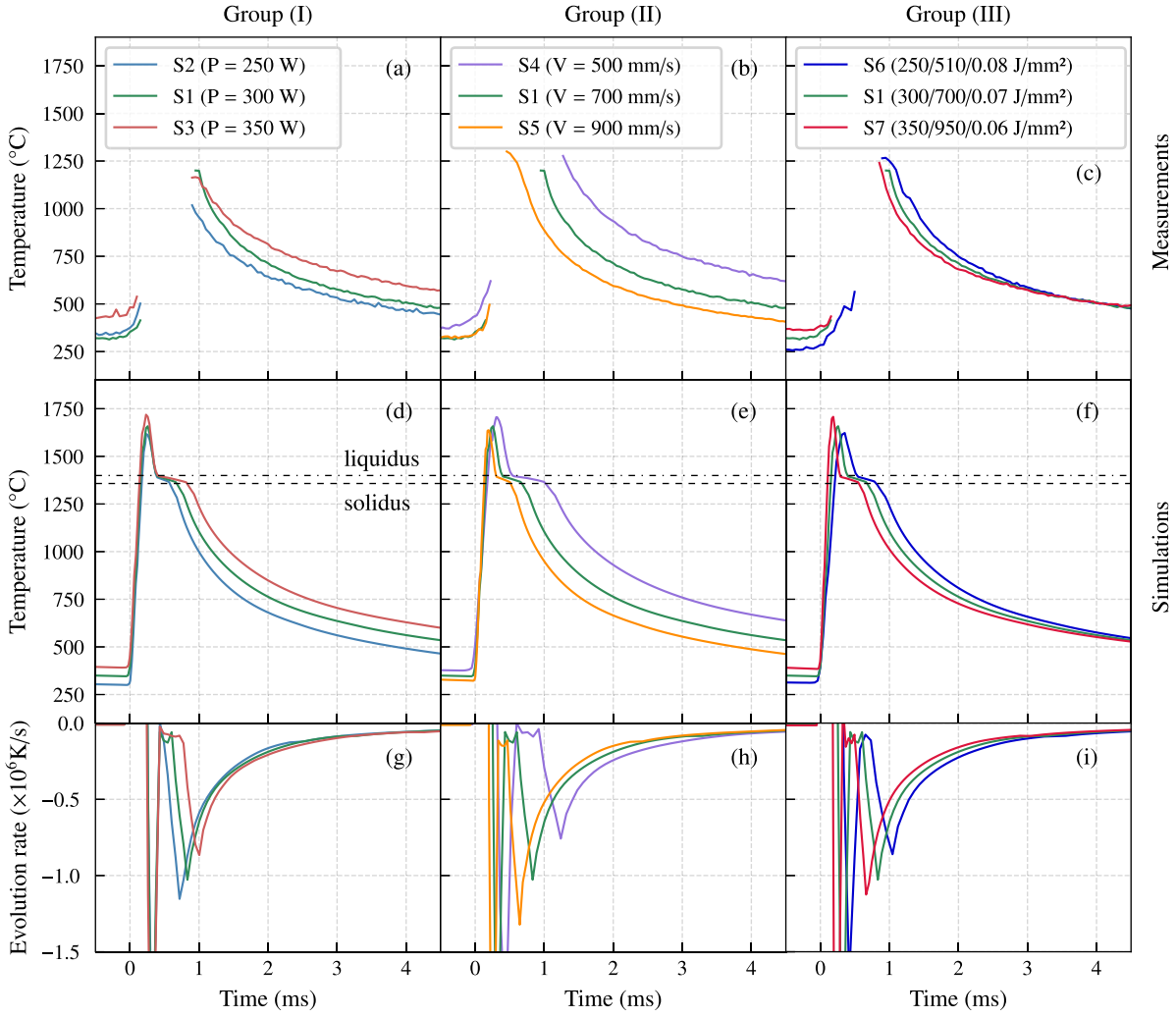

Fig. 5. Comparison of temperature profiles just after laser exposure, based on (a,b,c) XRD measurements and (d,e,f) model predictions for different process parameters. (g,h,i) The temperature evolution rates were calculated from the simulation results using cubic spline fits. The labels in (c) denote the values for $P/V/H$ for different samples. The simulated temperature histories were calculated as the average of 4 nodes around the (X:0 mm, Y:0.14 mm) coordinates with respect to the centre of laser scanned area.

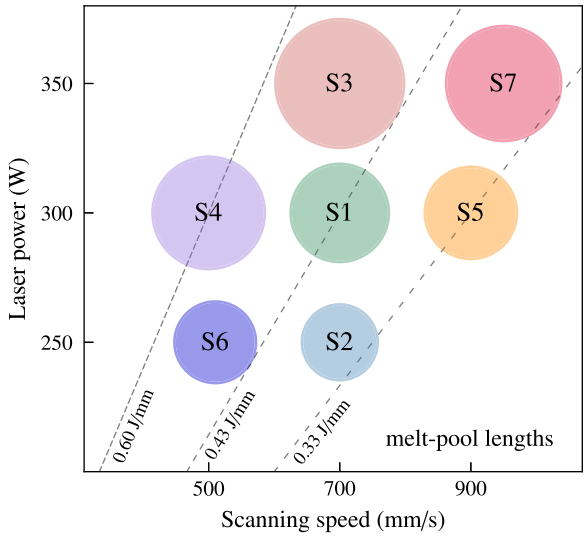

Fig. 6. Estimated melt-pool lengths based on simulated temperature histories. The circles are placed at coordinates corresponding to the laser power and scanning speed of the respective sample. The circle diameters are chosen proportional to the melt-pool lengths and the colours are adopted from Fig. 5. The dashed diagonal lines show contours of constant P/V ratios for 0.60/0.43/0.33 J/mm.

experimental campaign due to the single-point measurement limitation of the setup, the simulations offered the opportunity to compare temperature profiles at different locations of the same layer as presented in Fig. 8 for sample 1. Starting with the first layer (L01), the temperature histories at three different locations, namely the centres of the first track (T01), the middle track (T08), and the last track (T15) are shown in Fig. 8a. For T01, the section is initially at room temperature (25°C), and after laser exposure the deposited heat quickly dissipates through the cool build-plate with at a fast cooling rate (Fig. 8c). After scanning multiple tracks, the initial temperatures for T08 and T15 increase considerably to 295°C and 344°C, respectively. This local heating effect also slows the cooling process since the temperature difference between the process zone and the surrounding material is reduced. Furthermore, T01 and T15 reach the same maximum temperature while a −7.9 % relative drop is observed for T08. In essence, the high temperatures near the laser spot are not only affected by the local preheating, but also by the local geometry. In case of T08, the middle of the rectangle is fully connected to the build-plate which provides a low thermal resistance, while T01 and T15 are both located near the edges where heat transfer to the powder-bed is limited. Advancing to layer 11 (L11) in Fig. 8b, for T01 the material is near the ambient temperature before laser exposure, but for T08 and T15 the initial temperatures increase to 336°C and 524°C, respectively. While this local preheating is expected to decrease cooling rates, the local geometry plays a more important role. For example, even though the initial temperature for T08 is higher than T01, the lower thermal resistance in the middle of the layer compared to the edges substantially enhances heat dissipation as seen in Fig. 8d. The influence of boundary conditions induced by the local configuration of the solid material is also observed in higher maximum temperatures for T01 and T15 compared to the lower value for T08.

It should be noted that while FE simulations are powerful tools for understanding the heat transfer process in LPBF, they involve several simplifications in the presented setting. Most notably the lack of fluid dynamics consideration and mechanisms such as the Marangoni effect mean that the predicted temperatures above the solidus–liquidus range are highly uncertain. In addition, the reference state considered for the analysis of XRD data should ideally be stress-free, but our consideration does not fully meet this requirement. As a result, caution should be taken in interpretations based on the absolute values of measured and predicted temperatures. Nevertheless, the relative comparisons for different process conditions and at various locations remain valid and provide valuable insight into the inner workings of the thermal behaviour in LPBF, laying the foundation for further studies to delve deeper into these effects.

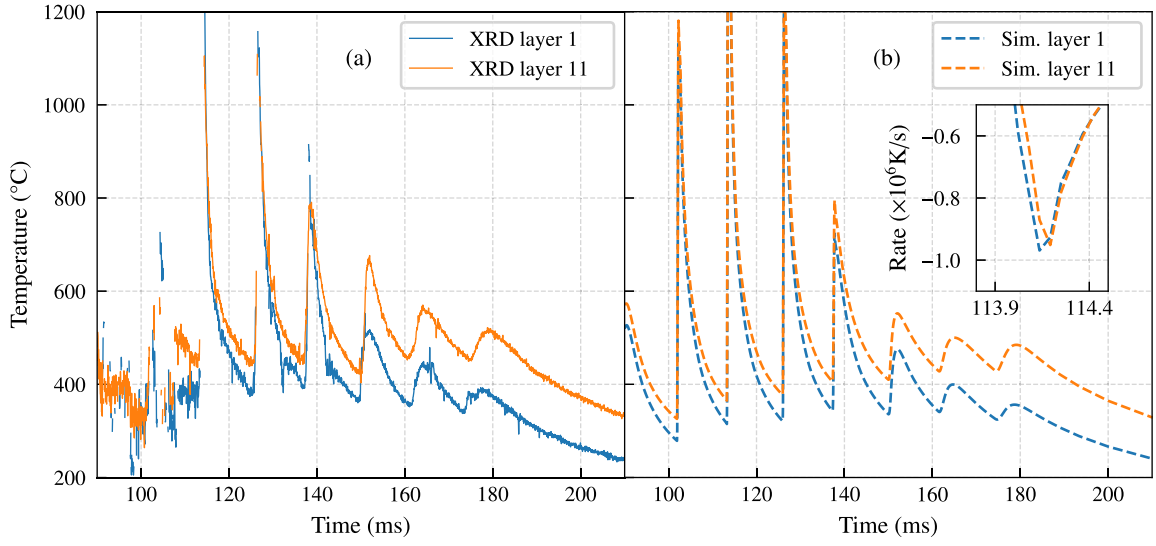

Fig. 7. Comparison of temperature profiles for layers 1 and 11 of sample 1 based on (a) measurements and (b) simulations. The inset in (b) shows that even the cooling rate after the largest temperature peak is impacted.

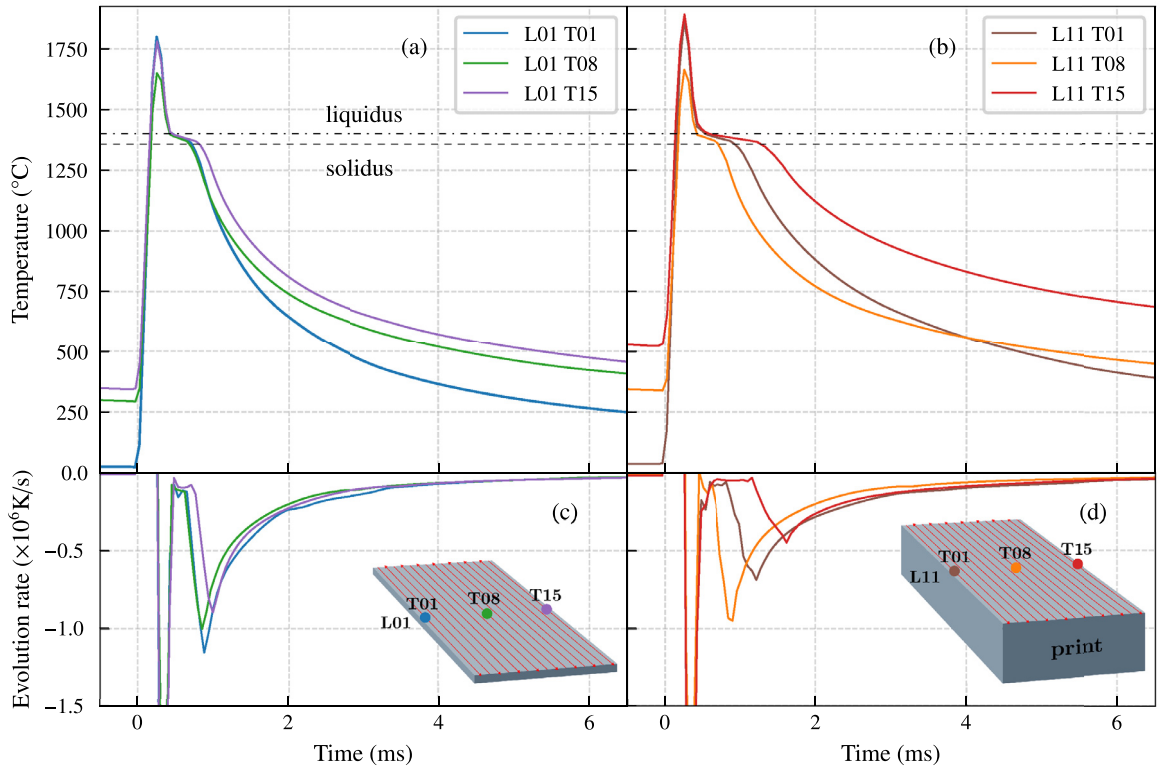

Fig. 8. Comparison of simulations temperature profiles for (a) layer 1 and (b) layer 11 of sample 1 at three different locations. (c,d) Corresponding evolution rate of temperatures for three tracks in layer 1 and 11, respectivly.

4. Conclusions

This work employed *operando* X-ray diffraction to measure the exposed temperature profiles by the laser heat source in LPBF of Hastelloy X and studied their sensitivity to process parameters and build height. FE thermal simulations were first validated based on the XRD measurement data and then used to complement the results by providing information about the cooling behaviour, melt-pool lengths and the heterogeneities in the temperature field within a build. The main contributions of this work can be stated as follows:

- The thermal histories for seven sets of process parameters were evaluated with experiments and simulations across laser powers, scanning speeds, and hatch distances.
- Higher energy densities, either from increasing the laser power or decreasing the scanning speed, increased the measured temperature levels and reduced the calculated cooling rates.
- The melt-pool length showed a high sensitivity to the laser power, and was less impacted by the changes in scanning speed.
- Comparison of the temperature histories among various tracks of different layers showed that increased thermal resistance between the LPBF process zone and the build-plate is responsible for higher local temperature levels and slower cooling behaviour.

Declaration of Competing Interest

The authors confirm that they do not have any conflict of interest with regards to contents of this work.

Data availability

Data will be made available on request.

Acknowledgments

Financial support by the Swiss National Science Foundation (SNSF; grant number 200551) is gratefully acknowledged. We acknowledge the Paul Scherrer Institut, Villigen, Switzerland for provision of synchrotron radiation beamtime at the microXAS beamline of the Swiss Light Source. All simulations were conducted on the ETH Euler cluster.

Supplementary material

Supplementary material associated with this article can be found, in the online version, at 10.1016/j.addlet.2023.100150

References

[1] M. Bayat, W. Dong, J. Thorborg, A.C. To, J.H. Hattel, A review of multi-scale and multi-physics simulations of metal additive manufacturing processes with focus on modeling strategies, Addit. Manuf. 47 (2021) 102278, doi:10.1016/j.addma.2021.102278.
[2] A. Vafadar, F. Guzzomi, A. Rassau, K. Hayward, Advances in metal additive manufacturing: areview of common processes, industrial applications, and current challenges, Appl. Sci. 11 (3) (2021) 1213, doi:10.3390/app11031213.
[3] Y. Yin, J. Zhang, J. Gao, Z. Zhang, Q. Han, Z. Zan, Laser powder bed fusion of ni-based hastelloy xsuperalloy: microstructure, anisotropic mechanical properties and strengthening mechanisms, Mater. Sci. Eng.: A 827 (2021) 142076, doi:10.1016/j.msea.2021.142076.
[4] O. Sanchez-Mata, J.A. Muñiz-Lerma, X. Wang, S.E. Atabay, M. Attarian Shandiz, M. Brochu, Microstructure and mechanical properties at room and elevated temperature of crack-free hastelloy x fabricated by laser powder bed fusion, Mater. Sci. Eng.: A 780 (2020) 139177, doi:10.1016/j.msea.2020.139177.
[5] N. Haghdadi, C. Ledermueller, H. Chen, Z. Chen, Q. Liu, X. Li, G. Rohrer, X. Liao, S. Ringer, S. Primig, Evolution of microstructure and mechanical properties in 2205 duplex stainless steels during additive manufacturing and heat treatment, Mater. Sci. Eng.: A 835 (2022) 142695, doi:10.1016/j.msea.2022.142695.
[6] W.E. Frazier, Metal additive manufacturing: a review, J. Mater. Eng. Perform. 23 (6) (2014) 1917–1928, doi:10.1007/s11665-014-0958-z.

[7] A. Keshavarzkermani, E. Marzbanrad, R. Esmaeilizadeh, Y. Mahmoodkhani, U. Ali, P.D. Enrique, N.Y. Zhou, A. Bonakdar, E. Toyserkani, An investigation into the effect of process parameters on melt pool geometry, cell spacing, and grain refinement during laser powder bed fusion, Opt. Laser Technol. 116 (2019) 83–91, doi:10.1016/j.optlastec.2019.03.012.

[8] A. Hilaire, E. Andrieu, X. Wu, High-temperature mechanical properties of alloy 718 produced by laser powder bed fusion with different processing parameters, Addit. Manuf. 26 (2019) 147–160, doi:10.1016/j.addma.2019.01.012.

[9] R. Esmaeilizadeh, A. Keshavarzkermani, U. Ali, B. Behravesh, A. Bonakdar, H. Jahed, E. Toyserkani, On the effect of laser powder-bed fusion process parameters on quasi-static and fatigue behaviour of hastelloy x: amicrostructure/defect interaction study, Addit. Manuf. 38 (2021) 101805, doi:10.1016/j.addma.2020.101805.

[10] S.I. Shahabad, U. Ali, Z. Zhang, A. Keshavarzkermani, R. Esmaeilizadeh, A. Bonakdar, E. Toyserkani, On the effect of thin-wall thickness on melt pool dimensions in laser powder-bed fusion of hastelloy x: numerical modeling and experimental validation, J. Manuf. Process. 75 (2022) 435–449, doi:10.1016/j.jmapro.2022.01.029.

[11] C.-H. Yu, R.L. Peng, V. Luzin, M. Sprengel, M. Calmunger, J.-E. Lundgren, H. Brodin, A. Kromm, J. Moverare, Thin-wall effects and anisotropic deformation mechanisms of an additively manufactured ni-based superalloy, Addit. Manuf. 36 (2020) 101672, doi:10.1016/j.addma.2020.101672.

[12] C.M. Pilgar, A.M. Fernandez, S. Lucarini, J. Segurado, Effect of printing direction and thickness on the mechanical behavior of SLM fabricated hastelloy-X, Int. J. Plast. 153 (2022) 103250, doi:10.1016/j.ijplas.2022.103250.

[13] A.J. Dunbar, E.R. Denlinger, J. Heigel, P. Michaleris, P. Guerrier, R. Martukanitz, T.W. Simpson, Development of experimental method for in situ distortion and temperature measurements during the laser powder bed fusion additive manufacturing process, Addit. Manuf. 12 (2016) 25–30, doi:10.1016/j.addma.2016.04.007.

[14] M. Masoomi, X. Gao, S.M. Thompson, N. Shamsaei, L. Bian, A. Elwany, Modeling, Simulation and Experimental Validation of Heat Transfer During Selective Laser Melting, ASME 2015 International Mechanical Engineering Congress and Exposition, American Society of Mechanical Engineers Digital Collection, 2016, doi:10.1115/IMECE2015-52165. V02AT02A007

[15] M. Chiumenti, E. Neiva, E. Salsi, M. Cervera, S. Badia, J. Moya, Z. Chen, C. Lee, C. Davies, Numerical modelling and experimental validation in selective laser melting, Addit. Manuf. 18 (2017) 171–185, doi:10.1016/j.addma.2017.09.002.

[16] A.M. Vest, D.R. St-Pierre, S. Rock, A.M. Maniatty, D.J. Lewis, S.J.A. Hocker, Thermocouple Temperature Measurements in Selective Laser Melting Additive Manufacturing, Technical Report, NASA, 2022.

[17] G. Mohr, S. Nowakowski, S.J. Altenburg, C. Maierhofer, K. Hilgenberg, Experimental determination of the emissivity of powder layers and bulk material in laser powder bed fusion using infrared thermography and thermocouples, Metals (Basel) 10 (11) (2020) 1546, doi:10.3390/met10111546.

[18] B. Lane, J. Heigel, R. Ricker, I. Zhirnov, V. Khromschenko, J. Weaver, T. Phan, M. Stoudt, S. Mekhontsev, L. Levine, Measurements of melt pool geometry and cooling rates of individual laser traces on IN625 bare plates, Integrat. Mater. Manuf. Innovat. 9 (1) (2020) 16–30, doi:10.1007/s40192-020-00169-1.

[19] P.A. Hooper, Melt pool temperature and cooling rates in laser powder bed fusion, Addit. Manuf. 22 (2018) 548–559, doi:10.1016/j.addma.2018.05.032.

[20] B. Lane, S. Moylan, E.P. Whitenton, L. Ma, Thermographic measurements of the commercial laser powder bed fusion process at NIST, Rapid. Prototyp. J. 22 (5) (2016) 778–787, doi:10.1108/RPJ-11-2015-0161.

[21] S. Hocine, H. Van Swygenhoven, S. Van Petegem, Verification of selective laser melting heat source models with operando X-ray diffraction data, Addit. Manuf. 37 (2021) 101747, doi:10.1016/j.addma.2020.101747.

[22] S. Hocine, S. Van Petegem, U. Frommherz, G. Tinti, N. Casati, D. Grolimund, H. Van Swygenhoven, A miniaturized selective laser melting device for operando X-ray diffraction studies, Addit. Manuf. 34 (2020) 101194, doi:10.1016/j.addma.2020.101194.

[23] F. Wang, Mechanical property study on rapid additive layer manufacture hastelloy® x alloy by selective laser melting technology, Int. J. Adv. Manuf. Technol. 58 (5–8) (2012) 545–551, doi:10.1007/s00170-011-3423-2.

[24] Q. Han, Y. Gu, H. Gu, Y. Yin, J. Song, Z. Zhang, S. Soe, Laser powder bed fusion of WC-reinforced hastelloy-X composite: microstructure and mechanical properties, J. Mater. Sci. 56 (2) (2021) 1768–1782, doi:10.1007/s10853-020-05327-6.

[25] T. Takeda, K. Kunitomi, T. Horie, K. Iwata, Feasibility study on the applicability of a diffusion-welded compact intermediate heat exchanger to next-generation high temperature gas-cooled reactor, Nucl. Eng. Des. 168 (1) (1997) 11–21, doi:10.1016/S0029-5493(96)01361-1.

[26] S. Hocine, H. Van Swygenhoven, S. Van Petegem, C.S.T. Chang, T. Maimaitiyili, G. Tinti, D. Ferreira Sanchez, D. Grolimund, N. Casati, Operando X-ray diffraction during laser 3D printing, Mater. Today (2019), doi:10.1016/j.mattod.2019.10.001.

[27] G. Tinti, A. Bergamaschi, S. Cartier, R. Dinapoli, D. Greiffenberg, I. Johnson, J.H. Jungmann-Smith, D. Mezza, A. Mozzanica, B. Schmitt, X. Shi, Performance of the EIGER single photon counting detector, J. Instrum. 10 (03) (2015), doi:10.1088/1748-0221/10/03/C03011. C03011–C03011

[28] Y. Mahmoodkhani, U. Ali, S. Imani Shahabad, A. Rani Kasinathan, R. Esmaeilizadeh, A. Keshavarzkermani, E. Marzbanrad, E. Toyserkani, On the measurement of effective powder layer thickness in laser powder-bed fusion additive manufacturing of metals, Progr. Addit. Manuf. 4 (2) (2019) 109–116, doi:10.1007/s40964-018-0064-0.

[29] D. Jansen, T. Hanemann, M. Radek, A. Rota, J. Schröpfer, M. Heilmaier, Development of actual powder layer height depending on nominal layer thicknesses and selection of laser parameters, J. Mater. Process. Technol. 298 (2021) 117305, doi:10.1016/j.jmatprotec.2021.117305.

[30] E.R. Denlinger, V. Jagdale, G.V. Srinivasan, T. El-Wardany, P. Michaleris, Thermal modeling of inconel 718 processed with powder bed fusion and experimental validation using in situ measurements, Addit. Manuf. 11 (2016) 7–15, doi:10.1016/j.addma.2016.03.003.

[31] E.R. Denlinger, M. Gouge, J. Irwin, P. Michaleris, Thermomechanical model development and in situ experimental validation of the laser powder-Bed fusion process, Addit. Manuf. 16 (2017) 73–80, doi:10.1016/j.addma.2017.05.001.

[32] D. Moser, M. Cullinan, J. Murthy, Multi-scale computational modeling of residual stress in selective laser melting with uncertainty quantification, Addit. Manuf. 29 (2019) 100770, doi:10.1016/j.addma.2019.06.021.

[33] Z. Luo, Y. Zhao, Efficient thermal finite element modeling of selective laser melting of inconel 718, Comput. Mech. 65 (3) (2020) 763–787, doi:10.1007/s00466-019-01794-0.

[34] N. An, G. Yang, K. Yang, J. Wang, M. Li, J. Zhou, Implementation of abaqus user subroutines and plugin for thermal analysis of powder-bed electron-beam-melting additive manufacturing process, Mater. Today Commun. 27 (2021) 102307, doi:10.1016/j.mtcomm.2021.102307.

[35] P. Scheel, R. Wrobel, B. Rheingans, T. Mayer, C. Leinenbach, E. Mazza, E. Hosseini, 3D Finite element thermal analysis of laser powder-bed fusion process: adaptive-local/global multiscale approach and experimental validation, Under Rev. (2023).

[36] S. Zhang, B. Lane, J. Whiting, K. Chou, On thermal properties of metallic powder in laser powder bed fusion additive manufacturing, J. Manuf. Process. 47 (2019) 382–392, doi:10.1016/j.jmapro.2019.09.012.

[37] J. Goldak, A. Chakravarti, M. Bibby, A new finite element model for welding heat sources, Metall. Trans. B 15 (2) (1984) 299–305, doi:10.1007/BF02667333.

[38] P. Michaleris, Modeling metal deposition in heat transfer analyses of additive manufacturing processes, Finite Elem. Anal. Des. 86 (2014) 51–60, doi:10.1016/j.finel.2014.04.003.

[39] J. Trapp, A.M. Rubenchik, G. Guss, M.J. Matthews, In situ absorptivity measurements of metallic powders during laser powder-bed fusion additive manufacturing, Appl. Mater. Today 9 (2017) 341–349, doi:10.1016/j.apmt.2017.08.006.

[40] S.I. Shahabad, Z. Zhang, A. Keshavarzkermani, U. Ali, Y. Mahmoodkhani, R. Esmaeilizadeh, A. Bonakdar, E. Toyserkani, Heat source model calibration for thermal analysis of laser powder-bed fusion, Int. J. Adv. Manuf. Technol. 106 (7) (2020) 3367–3379, doi:10.1007/s00170-019-04908-3.

[41] X. Gong, K. Chou, Microstructures of Inconel 718 by Selective Laser Melting, in: TMS 2015 144th Annual Meeting & Exhibition, Springer International Publishing, Cham, 2016, pp. 461–468, doi:10.1007/978-3-319-48127-2_58.